



Regular Article

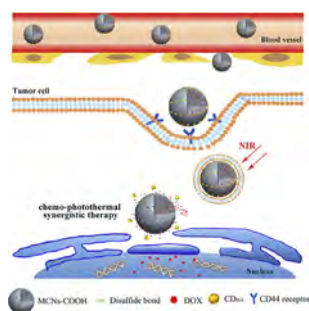
Multi-stimuli responsive nanosystem modified by tumor-targeted carbon dots for chemophototherapy synergistic therapy



Xiudan Wang, Xian Li, Yuling Mao, Da Wang, Qinfu Zhao, Siling Wang*

Department of Pharmaceutics, School of Pharmacy, Shenyang Pharmaceutical University, 103 Wenhua Road, Shenyang, Liaoning Province 110016, PR China

GRAPHICAL ABSTRACT



ARTICLE INFO

Article history:

Received 25 February 2019

Revised 3 May 2019

Accepted 25 May 2019

Available online 25 May 2019

Keywords:

Mesoporous carbon nanoparticles

Carbon dots

Tumor-targeted

Synergistic therapy

3D tumor spheroids

ABSTRACT

In this work, a tumor-targeted and multi-stimuli responsive drug delivery system combining infrared thermal imaging of cells with thermo-chemotherapy was developed. Oxidized mesoporous carbon nanoparticles (MCNs-COOH) with high photothermal conversion ability (photothermal transduction efficiency $\eta = 27.4\%$) in near-infrared (NIR) region were utilized to encapsulate doxorubicin (DOX). The outer surfaces of MCNs-COOH were capped with multifunctional carbon dots (CD_{HA}) as simultaneous smart gatekeepers, a tumor targeting moiety and a fluorescent probe. NIR laser irradiation killed cancer cells through NIR-light induced hyperthermia, facilitated chemotherapeutic drug release and enhanced the sensitivity of tumor cells to drugs. The therapeutic efficacy in two-dimensional (2D) and three-dimensional (3D) cells demonstrated that MC- CD_{HA} loading DOX (MC- CD_{HA}/DOX) had good chemo-photothermal synergistic antitumor effects (combination index of $CI = 0.448$). The biodistribution and pharmacodynamics experiments of MC- CD_{HA}/DOX in the 4T1 tumor model indicated that MCNs-COOH prolonged the residence time of DOX in tumor tissues and therefore actualized effective synergistic photothermal chemotherapy. By combining these excellent capabilities, the tumor-targeted and multi-stimuli responsive drug delivery system can be utilized as a visible nanoplatfor for chemophotothermal synergistic therapy.

© 2019 Elsevier Inc. All rights reserved.

1. Introduction

To date, chemotherapy has been widely applied as a dominating therapeutic method in oncology. However, the limitations of most

chemotherapeutic drugs must be solved, such as severe toxicity due to a non-tumor-specific targeting ability [1,2], poor bioavailability and large dosage requirements in the clinic. Therefore, one way to overcome these limitations is by developing tumor-targeted drug delivery systems (DDSs) [3–5]. In light of the multi-level complexities and variability of tumors, we sought to construct a multifaceted drug delivery system integrating

* Corresponding author.

E-mail address: silingwang@syphu.edu.cn (S. Wang).

diagnostics and chemotherapy with other therapeutic approaches to improve treatment efficacy and reduce side effects [6–9].

As an emerging physical therapy, photothermal therapy (PTT) eliminates tumor cells by converting near-infrared (NIR) light into cytotoxic heat [10–14]. NIR light, of wavelengths from 700 to 1100 nm, has received widespread attention because of its ability to trigger intelligent and efficient cancer therapy due to its typical characteristics, such as noninvasive application, good tissue transparency, accuracy and precision [15–17]. To date, UV and visible light have been applied to precisely activate drug release in drug delivery system based on existing cleavable moieties or bonds [17,18]. Comparing UV- and visible-light-triggered systems, NIR-triggered systems can remarkably induce drug release under light irradiation due to their ability to transform light into heat [19]. In this context, novel and intelligent drug delivery systems combining NIR light irradiation with other stimuli and even other therapeutic modalities to achieve synergistic anticancer effects have attracted widespread attention [20,21]. Hence, the challenge remains to construct smart nanoparticles that can be stimulated by NIR-light for precise cancer therapy.

Until now, sp^2 -hybridized carbon nanomaterials, such as zero-dimensional fullerene, one-dimensional carbon nanotubes [22–24], and two-dimensional grapheme [25–27], have been widely exploited for their use in photothermal cancer therapy due to their excellent photothermal conversion ability. As carbon derivatives, three-dimensional mesoporous carbon nanoparticles (MCNs) exhibit excellent potential in biomedicine, drug delivery, photothermal cancer therapy and many other applications [28,29]. The tunable pore size of MCNs is especially important for transporting various species between the surface and the core [30]. Meanwhile, MCNs are advantageous due to their drug loading capacity and PTT, with their dispersed sp^2 -hybridized pore walls contributing to drug loading and photothermal conversion [31].

Currently, many stimuli-responsive nanoparticles that can release guests in response to endogenous stimuli, such as the lysosomal pH [32], cytoplasmic glutathione (GSH) [33], enzymes [34] and reactive oxygen species (ROS) [10], have been fabricated to decrease premature drug release. Furthermore, some external stimuli, including light [35], heat [36], ultrasound [37], and magnetism [38], have also been exploited to accomplish on-demand drug release at the tumor site. Thus, the combination of intrinsic and external stimuli is beneficial for accurately and flexibly controlling intracellular drug delivery to achieve ideal anticancer efficiency [39].

In recent years, carbon dots (CDs), as a new class of photoluminescent (PL) material, have attracted considerable attention on account of their numerous merits, such as their good luminescence [40], high photostability, water dispersibility, excellent biocompatibility [41], and facile preparation and modification. Consequently, CDs have been extensively applied in sensing, theranostics, bioimaging [42], and catalysis. Recently, CDs with a self-targeting ability (labeled as CD_{HA}) were prepared by utilizing polymerizing reactions of citric acid (CA), hyaluronic acid (HA) polymers and ethylenediamine (EA), which can be selected as tumor targeting moieties owing to their ability to bind to CD44 receptors overexpressed on various cancer cells [43]. On the one hand, CD_{HA} can be used as gatekeepers to efficiently prevent drug leakage due to their diameters ranging from 2 nm to 10 nm. On the other hand, CD_{HA} can be hydrolyzed by intracellular hyaluronidases (HAases), which are abundant in tumor tissues. Moreover, the quenching and recovery of CD fluorescence play vital roles in visualization of the drug delivery process.

In this research, we fabricated a nanoplatfrom that has simultaneous multifunctional applications for photothermal therapy, chemotherapy and imaging via modifying mesoporous carbon NPs by loading doxorubicin (DOX) with tumor-targeting carbon

dots (CD_{HA}). As elucidated in Scheme 1, MCNs-COOH, as a drug carrier of the chemotherapeutic drug doxorubicin (DOX), can achieve synergistic anticancer efficacy by absorbing NIR. Then, MCNs-COOH are capped with CD_{HA} to further realize cell-specific targeting, location tracing and multi-stimuli responsive drug release. The morphology, size, optical properties and tumor targeting efficiency of CD_{HA} were researched. Furthermore, photothermal conversion capability, NIR imaging, drug loading, and drug release profiles of MC- CD_{HA} /DOX were investigated. On account of the outstanding NIR absorption and tumor intracellular tunable drug release of MC- CD_{HA} /DOX, cell viability experiments and in vivo photothermal therapy were explored to evaluate the synergistic therapeutic effects of the nanocomposites. Overall, the tumor-targeted and multi-stimuli responsive drug delivery system of MC- CD_{HA} /DOX will serve as a good theranostic agent for biomedical applications.

2. Materials and experimental conditions

2.1. Reagents

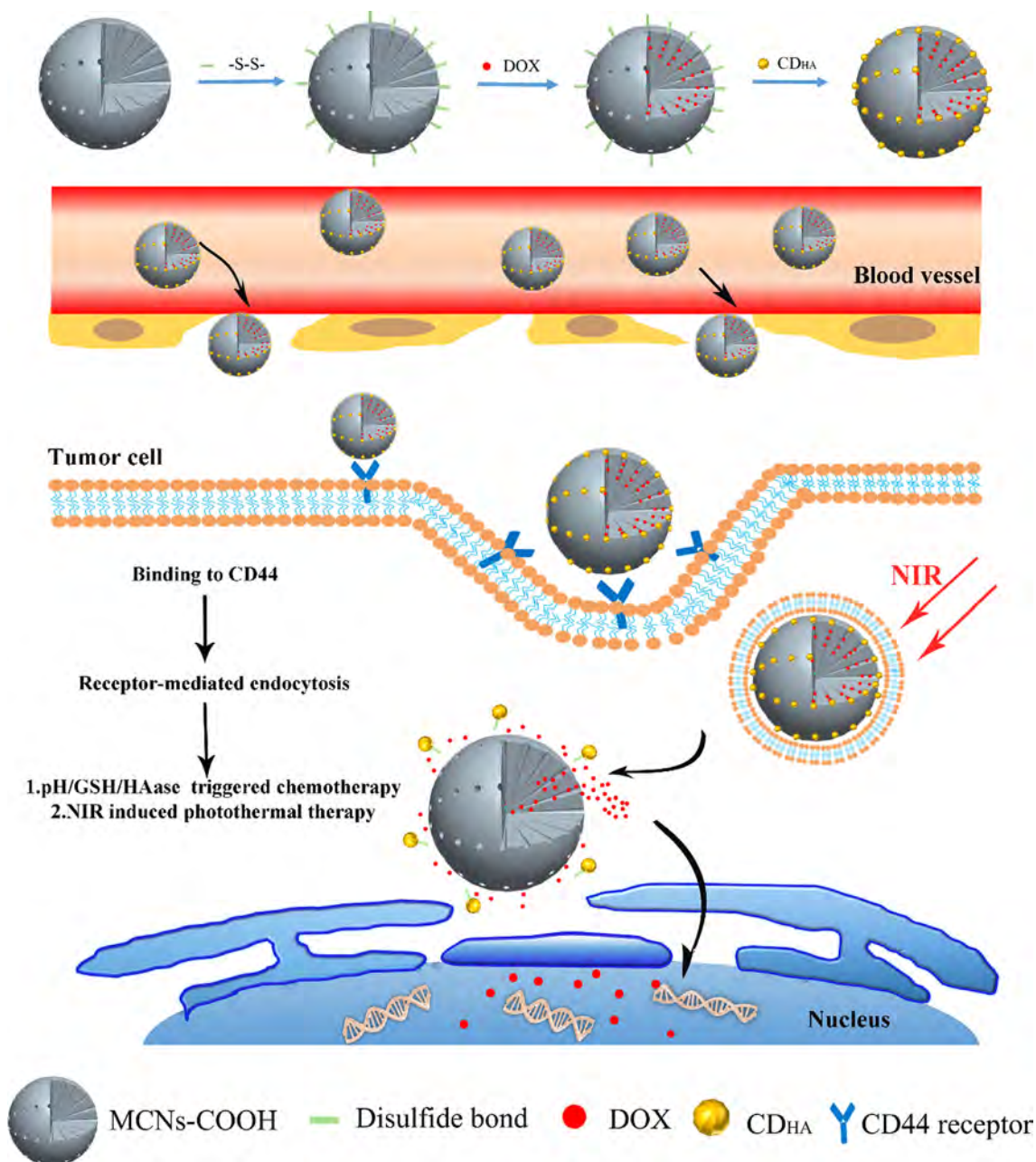
Citric acid (CA) and Ethylenediamine (EA) were supplied by Shan Dong Yu Wang Reagent Company (China). Cysteamine hydrochloride (98%), glutathione (GSH, 98%), N-(3-dimethylaminopropyl)-N-ethylcarbodiimide hydrochloride (EDC, 98%), N-hydroxysuccinimide (NHS, 98%) were obtained from Aladdin Chemical Inc. (Shanghai, China). Calcein-AM solution was purchased by Sigma-Aldrich (St. Louis, MO). Hyaluronidase (HAase, 300 U/mg), sodium hyaluronate (HA, 95%), doxorubicin hydrochloride (DOX, 98%), Fetal bovine serum (FBS), Roswell Park Memorial Institute (RPMI)-1640, Dulbecco's Modified Eagle Medium/Nutrient Mixture F-12 (DMEM/F-12), Hoechst 33,258 and propidium iodide (PI) solution were all attained from Dalian Meilun Biotechnology Co., Ltd. (Dalian, China). All other chemicals were of analytical grade and used without further purification.

2.2. Synthesis of MCNs-SS-NH₂

MCNs-COOH nanoparticles and S-(2-aminoethylthio)-2-thiopyridine hydrochloride (Py-SS-NH₂) were synthesized on the basis of a literature procedure [44]. EDC (200 mg) and NHS (100 mg) were added to N, N-dimethylformamide (50 mL) dispersion including MCNs-COOH (50 mg), and then, the mixture was stirred for 1 h to activate the carboxyl groups. Next, Py-SS-NH₂ (50 mg) was added to the above suspension and stirred at 40 °C for 36 h, and the reaction product (named as MCNs-SS-Py) was obtained by centrifugation. Subsequently, MCNs-SS-Py (50 mg) and cysteamine hydrochloride (50 mg) were dispersed in anhydrous ethanol (50 mL) and stirred at room temperature for 24 h. The resultant product (defined as MCNs-SS-NH₂) was segregated by centrifugation, washed with anhydrous ethanol and dried overnight under vacuum for further use.

2.3. Fabrication of MC- CD_{HA}

CD_{HA} was prepared by a facile green route [45], and the specific steps were as follows: 0.3 g HA, 3.0 g CA and 5 mL EA were mixed with 20 mL deionized water. Then, the above solution was transferred to a hydrothermal reactor and heated at 120 °C for 3 h. Finally, the resulting solution was dialyzed against deionized water for 8 h, freeze-dried and stored in a refrigerator. Next, the synthesized CD_{HA} was activated with EDC and NHS for 1 h, and subsequently, MCNs-SS-NH₂ was added before stirring for 36 h. Then, MC- CD_{HA} was obtained by centrifugation.



Scheme 1. Schematic illustration of the synthetic routes for the tumor-targeting, multi-stimuli responsive MC-CD_{HA}/DOX nanoplatform for cancer thermo-chemotherapy.

2.4. DOX-loaded delivery system and stimuli-responsive drug release *in vitro*

DOX was utilized as the model drug to study the drug loading capacity and controlled release profiles of the drug delivery system. The drug loading procedures were: mixing the DOX aqueous solution with MCNs-SS-NH₂ and continuously stirring for 12 h. Then, the solution was centrifuged and washed. CD_{HA} capped MCNs-SS-NH₂/DOX nanoparticles (labeled as MC-CD_{HA}/DOX) were prepared according to Section 2.3. Meanwhile, the eluent was collected at every step to quantitatively analyze the loading capacity by using UV-vis spectrophotometry at 480 nm.

The pH/redox/enzyme/NIR multi-stimuli responsive release profiles of DOX were evaluated by UV-vis spectroscopy at 480 nm. The release behavior of DOX from MC-CD_{HA}/DOX nanoparticles was assessed at different pH values (pH 5.0 and

pH 7.4 PBS) with/without GSH, HAase and NIR. The prepared MC-CD_{HA}/DOX nanoparticle samples were suspended in release media and shaken at 37 °C. At the designated time intervals, 1 mL aliquots of the release solution of different samples were withdrawn and then poured back into the release medium. For the laser irradiation groups, the samples were illuminated by an 808 nm NIR laser (2 W) with a spot diameter of 0.6 cm for 3 min at the selected time before measuring the absorbance of DOX.

2.5. Photothermal experiments

Photothermal heating of MC-CD_{HA} under NIR laser irradiation was measured by monitoring the temperature of the MC-CD_{HA} dispersions at various concentrations (5, 10, 25, 50, and 100 µg mL⁻¹) with water as the control. Furthermore, samples (50 µg mL⁻¹) were exposed to a NIR laser (808 nm) with different radiant

energies, and the temperature increase (ΔT) was recorded by an infrared thermal imaging camera. MC-CD_{HA} dispersions ($100 \mu\text{g mL}^{-1}$, 0.2 mL) were irradiated for 3 min (at a power density of 2 W), followed by natural cooling to room temperature without irradiation, which was repeated to evaluate the photothermal stability. The detailed calculations of the photothermal conversion efficiency are provided in the [supporting information](#).

2.6. Investigation of cellular photothermal effect induced by NIR

A549 and NIH-3T3 cells were seeded in 6-well plates at a density of 2.0×10^5 /well and incubated at 37 °C with 5% CO₂ for 24 h before they were incubated with MC-CD_{HA} at different concentrations of 10, 25, 50 and $100 \mu\text{g mL}^{-1}$ for 2 h. Then, the cells were completely rinsed with PBS, collected and irradiated with a NIR laser (2 W) for 3 min.

2.7. Cellular uptake

4T1 cells (including 4T1 tumor spheres) were cultured in RPMI-1640 medium, while NIH-3T3 and A549 cells were incubated with DMEM/F-12 medium under 5% CO₂ at 37 °C; all media contained 10% fetal bovine serum and 100 U mL^{-1} penicillin–streptomycin.

To verify the targeting ability of MC-CD_{HA}, NIH-3T3, A549 and 4T1 cells were incubated with MC-CD_{HA}, MC-CD_{HA}/DOX dispersions and the DOX solution for 2 h, the concentrations of which were equal to $5 \mu\text{g mL}^{-1}$ DOX. 4T1 cells with highly expressed CD44 receptors were used as another positive cell type [46]. Thereafter, the cells were immediately fixed, labeled with Hoechst and imaged by a laser scanning confocal fluorescence microscope. In a separate experiment, A549 cells and 4T1 cells were irradiated with the 2W NIR laser for 3 min after incubation with MC-CD_{HA}/DOX for 2 h to estimate the impact of NIR light on drug release. Then, the cells were rinsed, fixed, marked and characterized by fluorescence microscopy.

2.8. Cytotoxicity study in vitro

A549 and NIH-3T3 cells were seeded in 96-well plates at a density of 2×10^4 cells/well to evaluate the cellular cytotoxicity and study the synergistic effect in cancer therapy. After culturing for 24 h, cells were incubated with 100 μL of DMEM containing different concentrations of DOX, MC-CD_{HA} or MC-CD_{HA}/DOX for 24 h. Then, 50 μL of the MTT solution was added, and the mixture further incubated for 4 h to measure the cell viability by the MTT assay. To investigate the photothermal efficacy, A549 cells were

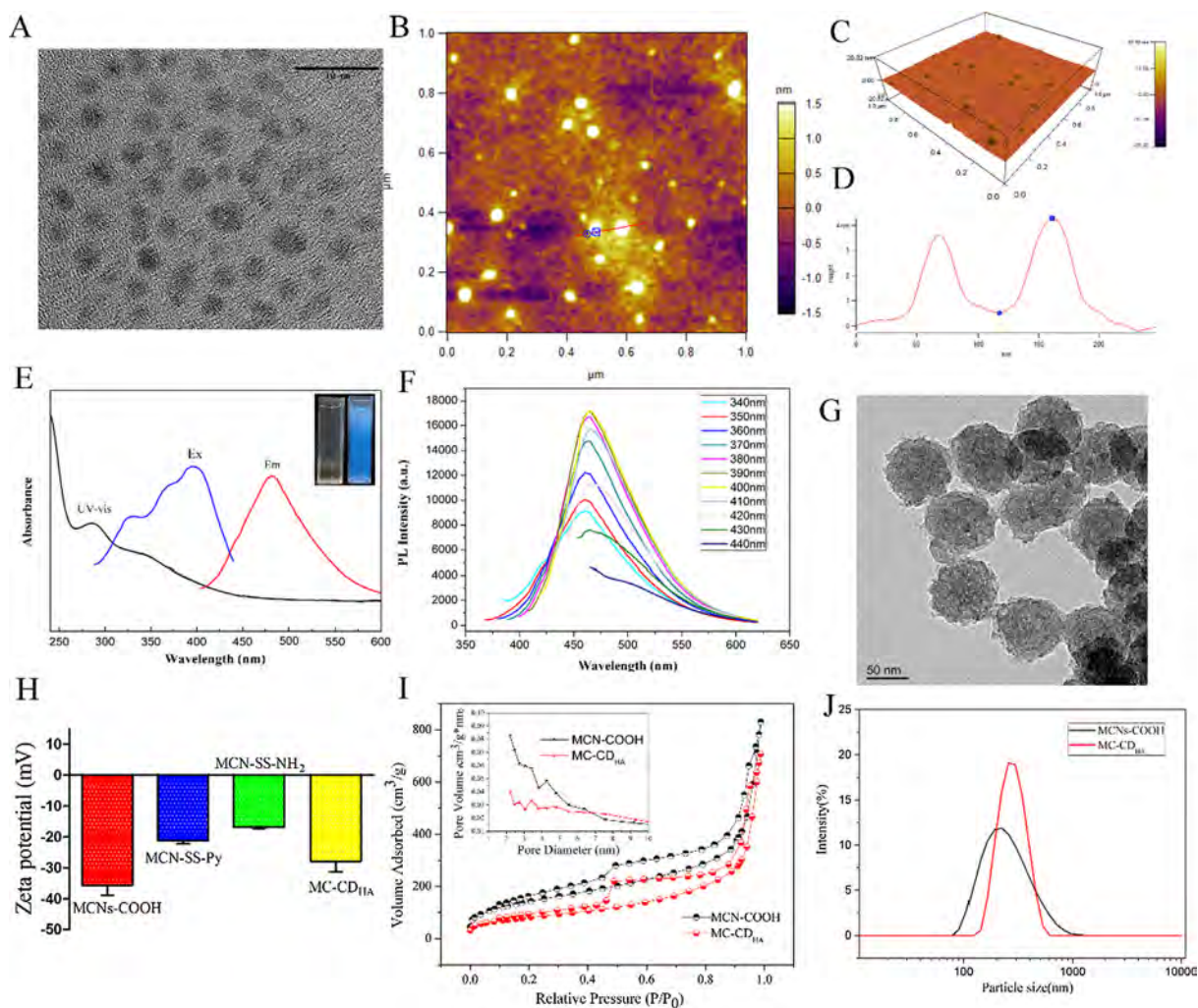


Fig. 1. (A) TEM images of CD_{HA}; (B) AFM images of CD_{HA}; (C) three-dimensional AFM results of CD_{HA}; (D) height profile along the line in (B); (E) UV–vis absorption spectra, excitation and emission spectra of CD_{HA} (insert: the photos of the aqueous solution of CD_{HA} under visible and 365 nm UV illumination); (F) PL emission spectra of CD_{HA} under different excitation wavelengths; (G) TEM image of MCNs-COOH; (H) corresponding Zeta potentials of MCNs-COOH, MCN-SS-Py, MCN-SS-NH₂ and MC-CD_{HA} (n = 3); (I) Nitrogen adsorption/desorption isotherms of MCNs-COOH and MC-CD_{HA} (insert: pore size distribution curves according to adsorption branch); and (J) size distributions of MCNs-COOH and MC-CD_{HA}.

irradiated with a NIR laser for 3 min before adding MTT. According to a previous study, the combination index was calculated to evaluate the therapeutic effect of combining chemotherapy and photothermal therapy.

The photothermal effects of MC-CD_{HA} on NIH-3T3 cells and 4T1 cells were also investigated. NIH-3T3 cells and 4T1 cells were cultured on 24-well cell culture dishes and incubated for 2 h. Next, they were illuminated with a laser and co-stained with calcein AM (green, live cells) and PI (red, dead cells) according to the manufacturer's instruction and then imaged by CLSM.

4T1 cell spheroids were prepared by using 96-well plates [47]. First, a 1% w/v agarose solution in distilled water was prepared and autoclaved. Then, the bottoms of 96-well plates were coated with 50 μ L agarose, and droplets (100 μ L) containing 3000 cells were added to each well. Subsequently, the plates were kept in an incubator with 5% CO₂ at 37 $^{\circ}$ C, and the cells were allowed to aggregate into round spheroids. After 3–5 days, multicellular tumor

spheroids of 4T1 cells with diameters of approximately 200–300 μ m were incubated with MC-CD_{HA} with or without laser irradiation for 3 min. The live and dead cells in the 3D tumor spheroids were distinguished by PI and calcein AM. To further investigate synergistic therapeutic effect of MC-CD_{HA}/DOX in 3D spheroid cells, 4T1 spheroids were incubated with different formulations for 24 h. Then, an inverted microscope equipped with a digital camera was used to study the size and morphology of the spheroids.

2.9. Hemocompatibility studies

Red blood cells (RBCs) from rabbits were centrifuged, washed and diluted with saline. Then, 1 mL of the diluted cell suspension was mixed with 1 mL of samples including different concentrations of MCNs-COOH and MC-CD_{HA}. After 4 h, the mixtures were centrifuged and the absorbance values of the supernatants were measured by UV–vis absorption spectrophotometer at 541 nm.

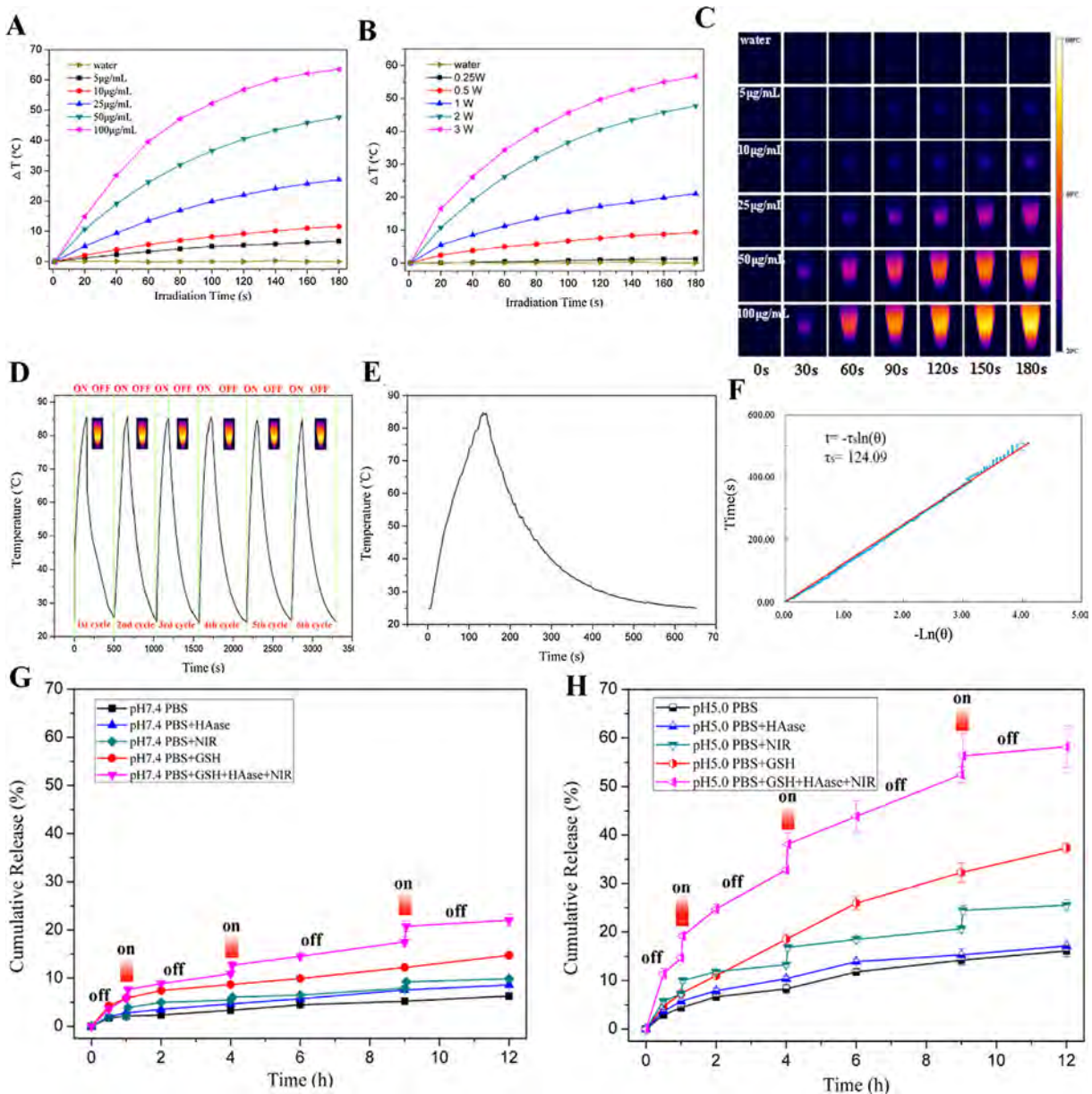


Fig. 2. (A) Temperature elevation of MC-CD_{HA} at different concentrations at a power density of 2 W and (C) the corresponding IRT images; (B) temperature elevation of the MC-CD_{HA} (50 μ g mL⁻¹) dependence on the light intensity; (D) photostability of MC-CD_{HA} (100 μ g mL⁻¹) over 6 irradiation cycles; (E) photothermal effect of an aqueous dispersion of MC-CD_{HA} (100 μ g mL⁻¹) under NIR laser irradiation (2 W); (F) linear time data versus $-\ln(\theta)$ obtained from the cooling stage of Fig. 2E; release profiles of MC-CD_{HA}/DOX with HAase, GSH and NIR irradiation at a power density of 2 W in (G) pH 7.4 and (H) pH 5.0 PBS (n = 3).

2.10. In vivo biodistribution

The cell surfaces of 4T1 cells had highly expressed CD44 receptors; therefore, 4T1 tumor-bearing mice were used to study the in vivo performance. Female Balb/c mice (18–22 g) were used to establish the 4T1 tumor model by a subcutaneous injection of 4T1 tumor cells (5×10^4 cells in 100 μ L of PBS) into the right rear flank. The tumor sizes were measured based on a Vernier caliper and calculated as the volume = (tumor length) \times (tumor width)²/2. When the tumor size reached approximately 150 mm³, 4T1 tumor-bearing mice were divided into several groups and intravenously injected separately with 100 μ L of free DOX and MC-CD_{HA}/DOX at a DOX dose of 5 mg/kg. Mice were euthanized and sacrificed at the given times (2, 6, and 12 h); then, the tumors and major organs (heart, liver, spleen, lung, and kidney) were collected and imaged by an IVIS in vivo imaging system. Finally, the mean fluorescence intensity of DOX in tissues were determined by the Bruker MI SE software.

2.11. Combination therapy in vivo

Tumor-bearing mice were randomly divided into five groups (five mice per group) and separately received treatment with normal saline (control), free DOX, MC-CD_{HA} plus laser irradiation, and MC-CD_{HA}/DOX both with and without laser irradiation via the tail vein. The 808 nm laser irradiation was carried out on tumor regions for 3 min at a power density of 2 W. During the irradiation period, images of mice and the temperatures of tumor sites were recorded by an IR thermal camera. The tumor volumes and body weights of these mice were measured once every 2 d for 15 consecutive days. At the end of the treatment, the major organs (heart, liver, spleen, lung, and kidney) and tumors were collected for hematoxylin and eosin (H&E) staining for further histological examinations.

2.12. Characterizations

Nitrogen adsorption-desorption isotherms based on BJH model were collected on an adsorption analyzer (V-Sorb 2800P, Gold APP Instrument Corporation, Beijing, China). The morphologies of car-

ries were observed by transmission electron microscopy (TEM) (Tecnai G² F30, FEI, Eindhoven, Netherlands). The size distribution and mean diameter were measured by using a Particle Size Analyzer Nicomp 380 (Particle Sizing Systems, USA). Spectrophotometry measurements were conducted on a UV-vis spectrometer (UNIC, Shanghai, China) at room temperature. The fluorescence spectra were characterized on a SpectraMax M5 multifunctional microplate reader (Molecular Devices, USA).

3. Results and discussion

3.1. Preparation and characterization of CD_{HA}

CD_{HA} were facilely prepared through hydrothermal heating an EA solution that included citric acid and hyaluronic acid at 120 °C for 3 h in an autoclave, followed by centrifugation and dialysis purification [45]. Then, TEM and atomic force microscope (AFM) were applied to characterize the size and morphology of CD_{HA}. As shown in Fig. 1A, CD_{HA} displayed a mono-dispersed state and uniform spherical morphology with an average size of approximately 4 nm, as detected by TEM. As shown in Fig. 1B, the AFM 3D image and topography image further showed that the morphology of CD_{HA} was a spherical structure with similar particle heights of approximately 4 nm, agreeing with the TEM results. Therefore, it can be speculated that CD_{HA} can act as gatekeeper and impede the premature release of a loaded drug. Subsequently, the optical properties of CD_{HA} were investigated to determine whether CD_{HA} was suitable for biological labelling and imaging. As shown in Fig. 1E and F, CD_{HA} exhibited wide absorption bands from 300 nm and 400 nm, demonstrating the presence of a π - π^* transition of chromophores and n- π^* transition of carbonyl groups.

3.2. Preparation and characterization of MC-CD_{HA}/DOX

The synthetic strategy for MC-CD_{HA}/DOX is illustrated in Scheme 1. The MCNs-COOH were fabricated according to our previous report [44]. As shown in Fig. 1G, TEM showed that MCNs-COOH possessed a narrow size distribution with a particle diameter of 100 nm and abundant mesoporous pores, which were suitable for penetrating cells and achieving efficient drug loading.

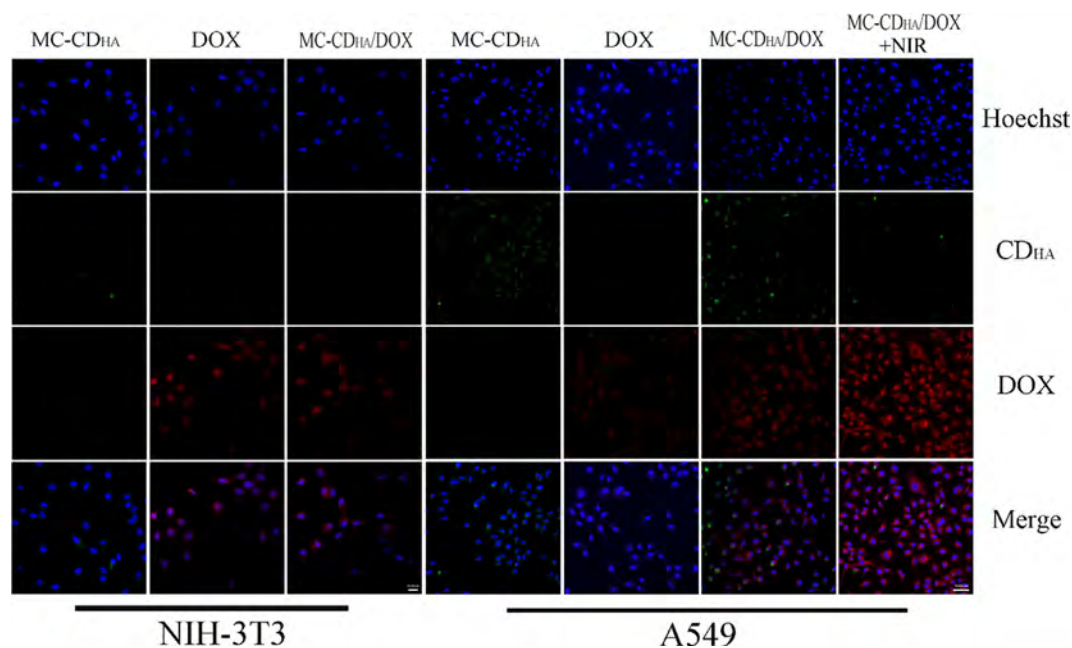


Fig. 3. CLSM images of NIH-3T3 and A549 cells cultivated with MC-CD_{HA}, DOX, MC-CD_{HA}/DOX and MC-CD_{HA}/DOX under NIR irradiation for 2 h.

The Zeta potential (Fig. 1H), N_2 adsorption–desorption isotherms (Fig. 1I and Table S1) and dynamic laser scattering (Figs. 1J and S1) results all confirmed the modification of CD_{HA} on the surface of MCNs-COOH.

The drug loading capacity of MC- CD_{HA} /DOX reached up to 28% due to the strong adsorption ability between MCNs-COOH and DOX based on UV–Vis absorption measurements. As indicated in Fig. S2, no apparent crystalline peaks of DOX were observed owing to the restriction of the mesoporous structure of MCNs-COOH. As shown in Fig. S3, free DOX could emit red fluorescence under 480 nm excitation, whereas fluorescence was quenched when DOX entered the pores inside of MC- CD_{HA} . Fig. S4 shows that MC- CD_{HA} exhibited good stability in pH 7.4 PBS and water compared to MCNs-COOH. Therefore, CD_{HA} is also able to improve

the dispersity and stability of MCNs-COOH apart from trapping the guest within the mesoporous channels during capping.

3.3. Photothermal properties of MC- CD_{HA}

To shed light on the good photothermal conversion capability of MC- CD_{HA} , their absorption in the near infrared light region was first investigated. Fig. S5 shows that MC- CD_{HA} exhibited relatively strong NIR absorption at 808 nm. MC- CD_{HA} suspensions of various concentrations were irradiated: $100 \mu\text{g mL}^{-1}$ MC- CD_{HA} suspension could be heated up to 88°C , whereas pure water had no apparent temperature increase under the same condition (Fig. 2A). Furthermore, the temperature rise followed a laser-power-dependent manner, as indicated in Fig. 2B. Meanwhile, Fig. 2C shows the

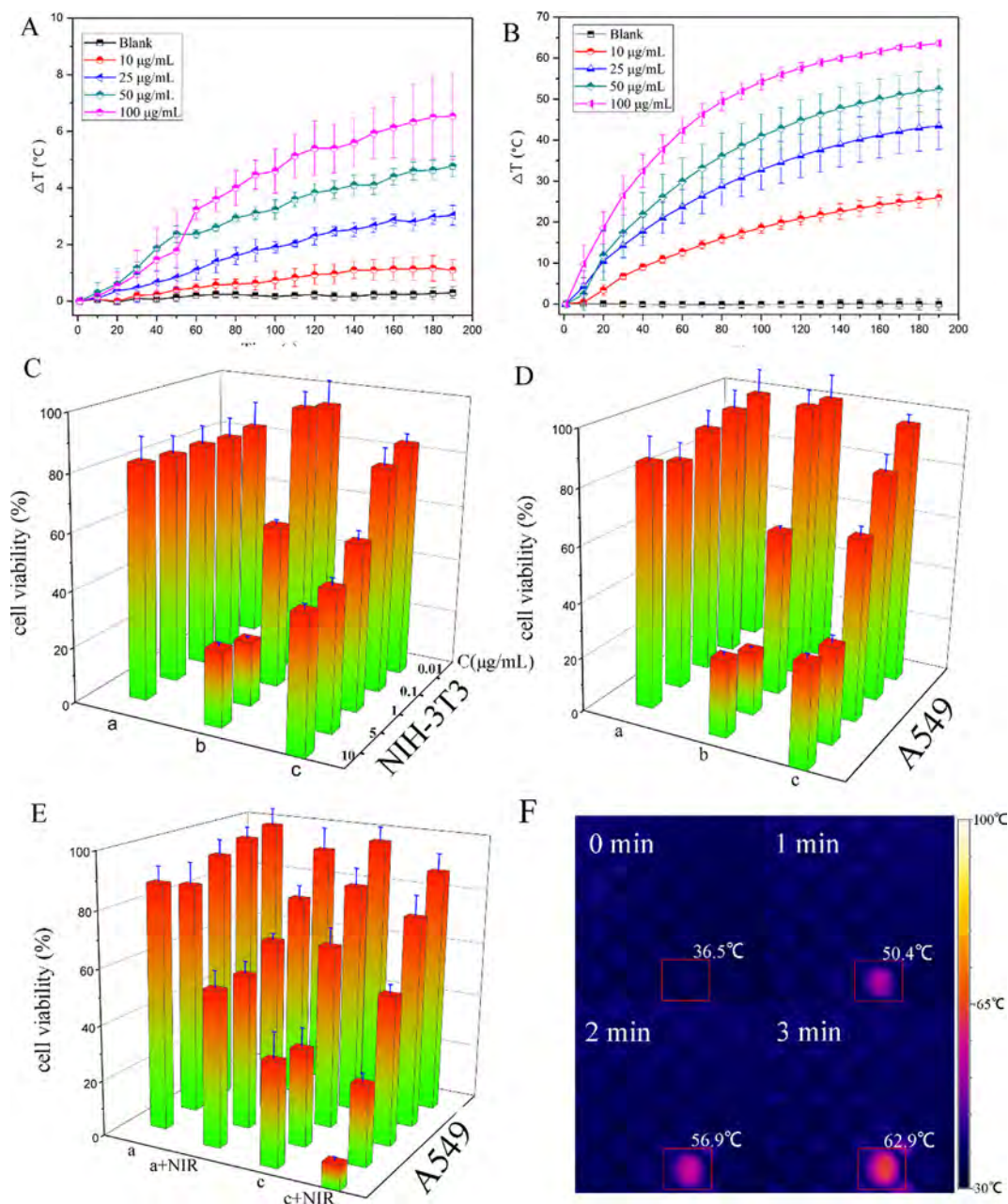


Fig. 4. NIR-induced cellular photothermal effect of NIH-3T3 (A) and A549 (B) cells incubated with different concentrations of MC- CD_{HA} ($n = 3$); cytotoxicity assays ($n = 5$) of NIH-3T3 (C) and A549 cells (D) incubated with MC- CD_{HA} (a), DOX (b), and MC- CD_{HA} /DOX (c) for 24 h; (E) viability of A549 cells incubated with MC- CD_{HA} (a), MC- CD_{HA} /DOX (c), and MC- CD_{HA} with NIR (a + NIR) and MC- CD_{HA} /DOX with NIR (c + NIR); (F) the temperature and corresponding infrared thermal images of a 96-well cell-culture plate containing A549 cells and MC- CD_{HA} at 0, 1, 2 and 3 min after laser irradiation.

Table 1

IC₅₀ values of MC-CD_{HA}, DOX, and MC-CD_{HA}/DOX samples with/without NIR irradiation against NIH-3T3 and A549 cells.

Preparations	IC ₅₀ (μg/mL)		
	NIH-3T3	A549	A549 + NIR
MC-CD _{HA}	–	–	13.837
DOX	1.654	1.834	
MC-CD _{HA} /DOX	5.604	2.631	0.726

excellent IR thermal (IRT) imaging property, which was ascribed to the high thermal contrast produced by MC-CD_{HA}. As shown in Fig. 2D, the excellent photostability of MC-CD_{HA} (100 μg mL⁻¹) was verified by the observation that the temperature elevation of MC-CD_{HA} did not markedly change upon multiple irradiation cycles. Meanwhile, the size and Zeta potential of MC-CD_{HA} were perfectly maintained after exposure to NIR, which also confirmed the property, as shown in Fig. S6. Furthermore, the photothermal conversion efficiency (η) was calculated to be 27.4% according to the obtained data (Fig. 2E and F). The outstanding efficiency and stability of the photothermal conversion supported MC-CD_{HA} as a promising PTT carrier.

3.4. Stimuli-responsive drug release and dissociation

The drug release capability of MC-CD_{HA}/DOX was evaluated in response to acidic, HAase, and reductive stimuli, as well as a NIR-light-triggered thermal stimulus. Compared with the physiological environment, the release percentage of DOX slightly increased under acidic conditions within 12 h, as shown in Fig. 2G and H. Moreover, the release percentage of DOX increased in the presence of HAase within 12 h both in pH 5.0 and pH 7.4 PBS, which was

ascribed to the situation in which the gatekeeper CD_{HA} could be degraded by hyaluronidase and thus facilitated DOX diffusion from the mesopores into the medium. Next, the release behaviors of MC-CD_{HA}/DOX under multiple irradiation treatments were evaluated. The further increased release of DOX when exposed to NIR irradiation could be explained by the heat generated from MC-CD_{HA}, thus speeding up molecular movement and promoting drug diffusion. In addition, the maximized release of DOX (58%) was observed at pH 5.0 in the presence of GSH, HAase and NIR light irradiation.

In addition, to certify the function of CD_{HA} as a gatekeeper, the fluorescence spectra of the supernatant of CD_{HA} from MC-CD_{HA} without DOX were recorded after the addition of 0 mM, 3 mM and 10 mM of GSH. As shown in Fig. S7, there was no fluorescence observed after adding 0 mM GSH, while the fluorescence of CD_{HA} was with the elevated concentrations of GSH. The quenching and recovery of fluorescence offered the ability to monitor the drug release cascade.

All of the above results revealed that CD_{HA}, acting as a gatekeeper, exhibited a decent capping efficiency and multi-responsive drug release profile. These findings provide opportunities for on-demand cargo delivery systems to improve antitumor efficacy.

3.5. Cellular uptake

To monitor the receptor-mediated cellular uptake capability of MC-CD_{HA}/DOX nanoparticles, the gatekeeper CD_{HA} and encapsulated DOX were simultaneously used as two fluorescence probes to judge the targeting effect by confocal microscopy. As observed in Fig. 3, only red fluorescence (DOX) and blue fluorescence were detected when the two cell lines were cultured with free DOX. The green fluorescence from CD_{HA} was more apparent in A549 cells

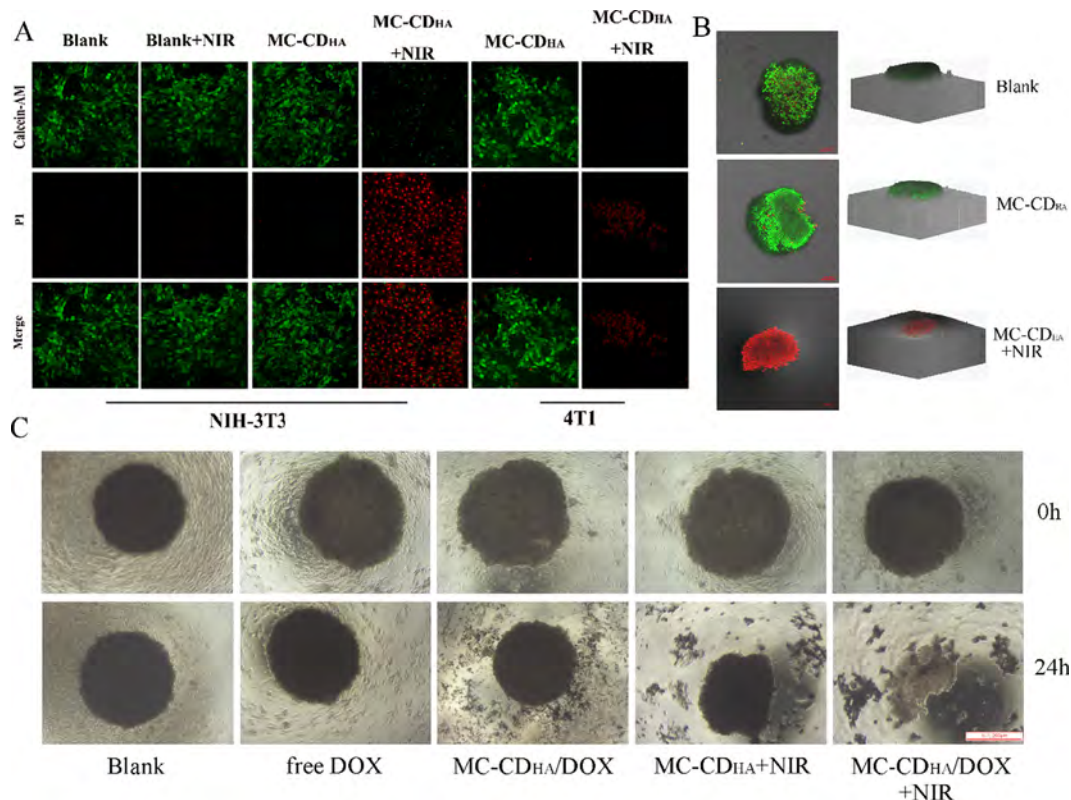


Fig. 5. (A) Confocal photographs of calcein AM and propidium iodide co-stained NIH-3T3 and 4T1 cells; (B) live-dead cell assays for 4T1 cell spheroids after different treatments; (C) optical images of 4T1 tumor spheres treated with different preparations at 0 h and 24 h.

than in NIH-3T3 cells, which proved that more MC-CD_{HA} were delivered into A549 cells with the help of overexpressed CD44 receptors. This result was further verified by the observation that strong red fluorescent signals were detected in A549 cells, whereas a weaker red fluorescent signal was observed in NIH-3T3 cells after they were treated with MC-CD_{HA}/DOX. The results suggested that the cells without overexpressed CD44 receptors were not subjected to the invasion of nanoparticles. Encouraged by the NIR-responsive release experiments of MC-CD_{HA}/DOX, we studied whether drug release in A549 cells was enhanced. In comparison to those without irradiation, a considerably enhanced red fluorescence accumulated in the cytoplasm after laser irradiation. As shown in Fig. S8, 4T1 cells, as another positive cell type, produced the same experimental phenomenon as A549 cells, which could be explained by the fact that the molecules moved faster due to the elevated temperature and easily crossed the cell membrane. As seen from the results, MC-CD_{HA}/DOX is anticipated to exhibit much higher cytotoxicity to tumor cells and can target and control on-demand release *in vitro*.

3.6. Cellular photothermal effect studies

The high photothermal conversion efficiency of MC-CD_{HA} prompted us to evaluate the cellular photothermal effect based on MC-CD_{HA}. As shown in Fig. 4A and B, there were obvious temperature increases with the increasing concentrations of MC-

CD_{HA}, while the temperature of blank cells did not apparently change after NIR irradiation. Meanwhile, the increased temperature of A549 cells was relatively higher than that of NIH-3T3 cells when they were cultured with MC-CD_{HA} at the same concentration, indicating a larger uptake of MC-CD_{HA} by A549 cells than that by NIH-3T3 cells due to the difference in CD44 receptor expression. The remarkable photothermal conversion efficiency and selectivity in treating cancer were distinctly shown by the cellular photothermal effect.

3.7. *In vitro* cytotoxicity testing

To estimate the biocompatibility and antitumor ability of the prepared MC-CD_{HA}, MC-CD_{HA}/DOX and free DOX *in vitro*, the MTT assay was applied to investigate the therapeutic effects of MC-CD_{HA}/DOX against two cell lines, A549 and NIH-3T3, under different treatments. As shown in Fig. 4C and D, MC-CD_{HA} exhibited negligible toxicity towards A549 and NIH-3T3 at different concentrations, revealing the excellent biocompatibility and security of the prepared MC-CD_{HA}. Additionally, the dose-dependent cytotoxicities of free DOX and MC-CD_{HA}/DOX against A549 and NIH-3T3 cells were also examined. MC-CD_{HA}/DOX resulted in more severe cytotoxicity against A549 cells ($IC_{50} = 2.631 \mu\text{g mL}^{-1}$) than against NIH-3T3 cells ($IC_{50} = 5.604 \mu\text{g mL}^{-1}$), which further confirmed that the death of cells was caused by the increased cellular uptake of MC-CD_{HA}/DOX inside cancer cells via receptor mediated endocytosis.

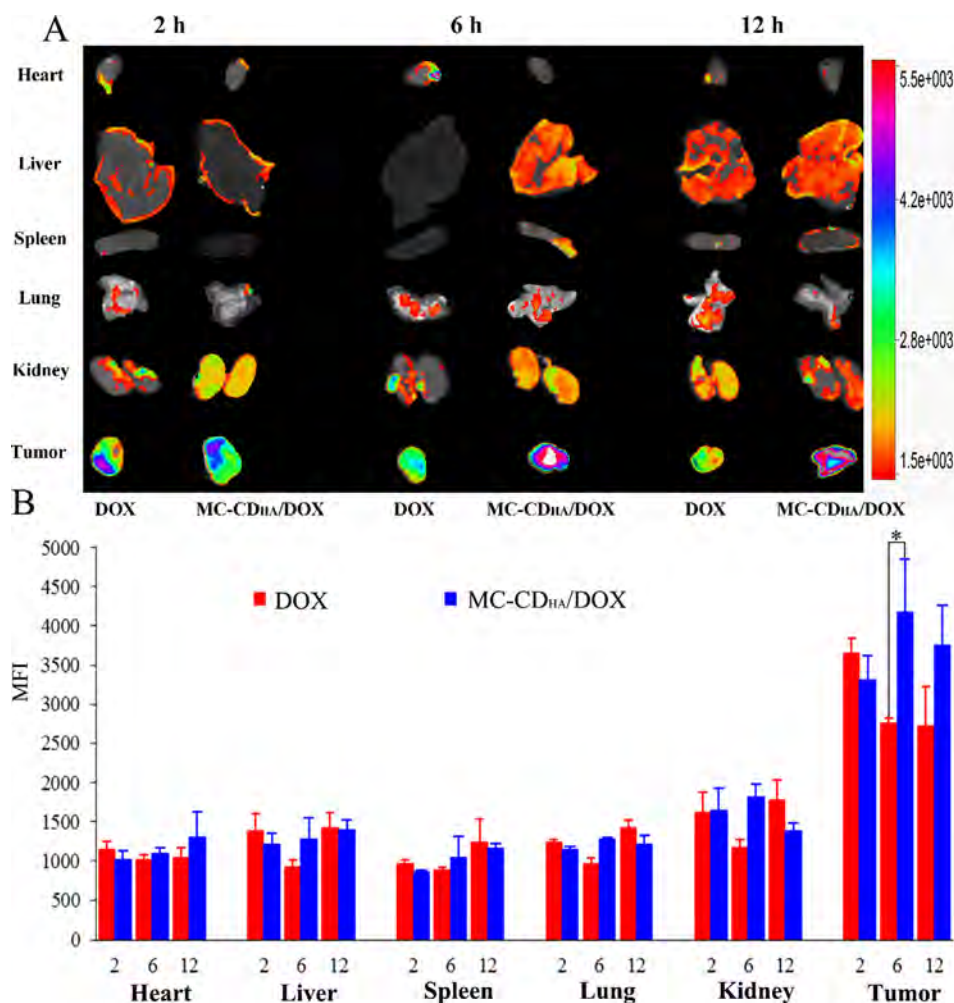


Fig. 6. (A) Fluorescence imaging of isolated organs at 2, 6 and 12 h after administration of free DOX and MC-CD_{HA}/DOX; (B) fluorescence semi-quantification of the DOX biodistribution in mouse tissues with 4T1 tumors collected at 2, 6 and 12 h postinjection ($n = 3$).

sis. For NIH-3T3, uptake of MC-CD_{HA}/DOX was reduced owing to the negative expression of CD44 receptors, which reduced the side effects. By contrast, free DOX showed no significant difference in cytotoxicity against A549 and NIH-3T3 cells. MC-CD_{HA}/DOX as a targeted drug delivery system is superior to free DOX in treating cancer.

As shown in Fig. 4E and Table 1, the value of IC₅₀ markedly decreased for A549 cells under NIR laser irradiation, which certified that MC-CD_{HA} have the ability to transform the NIR light into heat to ablate cancer cells. In addition, only wells containing MC-CD_{HA} could be highly heated (62.9 °C), and they produced bright thermal images under irradiation, implying that MC-CD_{HA} could also serve as a prominent contrast agent for infrared thermal imaging and realize real-time monitoring of thermal dynamics in PTT (Fig. 4F). The combination index (CI) used to assess the synergistic effect of the combination therapy was calculated as 0.448, which implied that the combination of chemotherapy and photothermal therapy based on MC-CD_{HA}/DOX had a good synergistic effect [48](CI > 1, =1, or < 1, indicates antagonistic, additive, or synergistic effects, respectively). This result can be explained by the observation that the temperature rise can not only kill tumor cells but also increase cellular sensitivity to chemotherapeutic drugs, thus triggering maximal cytotoxicity.

To study the feasibility of MC-CD_{HA} as a PTT agent for cancer therapy, NIH-3T3 and 4T1 cells were cocultured with MC-CD_{HA} dispersions and illuminated by 808 nm laser, followed by staining with calcein AM and PI. As shown in Fig. 5A, cells treated with either MC-CD_{HA} or the laser alone showed negligible cell death, the same as the blank group. By contrast, cells treated with MC-CD_{HA} and NIR irradiation simultaneously exhibited a red fluorescence signal, suggesting that the majority of cells were killed. Compared with NIH-3T3 cells, the amount of 4T1 cells illuminated with NIR remarkably decreased, which might be ascribed to cell death and washing away with PBS. Moreover, a similar phenomenon

was also observed for the 3D tumor spheroids treated with MC-CD_{HA} in the presence or absence of laser irradiation (Fig. 5B).

The therapeutic effects mediated by MC-CD_{HA}/DOX under laser irradiation were investigated in 4T1 spheroids (Fig. 5C). Our microscopic analyses showed that the average diameters of spheroids under the treatments were all smaller than that of the control group after 24 h. Among these treatments, MC-CD_{HA}/DOX with laser irradiation induced a pronounced destruction of the spheroids, suggesting that almost all cancer cells were killed. These findings demonstrated that MC-CD_{HA}/DOX possessed great promise as an effective tumor targeting and PTT agent for in vivo tumor therapy.

3.8. Biodistribution study

In cancer chemotherapy, the rapid clearance of chemotherapeutic drugs from solid tumors is one reason for treatment failure. Nanoparticles loaded with chemotherapeutic drugs prolonged the retention of drugs in the tumor through the enhanced permeability and retention (EPR) effect [49]. The biodistribution of DOX in 4T1 tumor-bearing mice after an intravenous injection of free DOX and MC-CD_{HA}/DOX was examined to evaluate the tumor retention capability. As shown in Fig. 6A and 6B, the mean fluorescence intensity (MFI) of DOX in tumors was reduced after injection of free DOX at 2 h by virtue of rapid elimination in vivo. Compared to free DOX, MC-CD_{HA}/DOX presented stronger fluorescent signals in tumors within 12 h, which was likely attributed to the enhanced permeability and retention (EPR) effect caused by the MC-CD_{HA} nanosystem.

3.9. Chemotherapy/PTT efficacy of MC-CD_{HA}/DOX in vivo

Motivated by the synergistic antitumor effect in vitro and enhanced tumor accumulation, we further investigated the antitu-

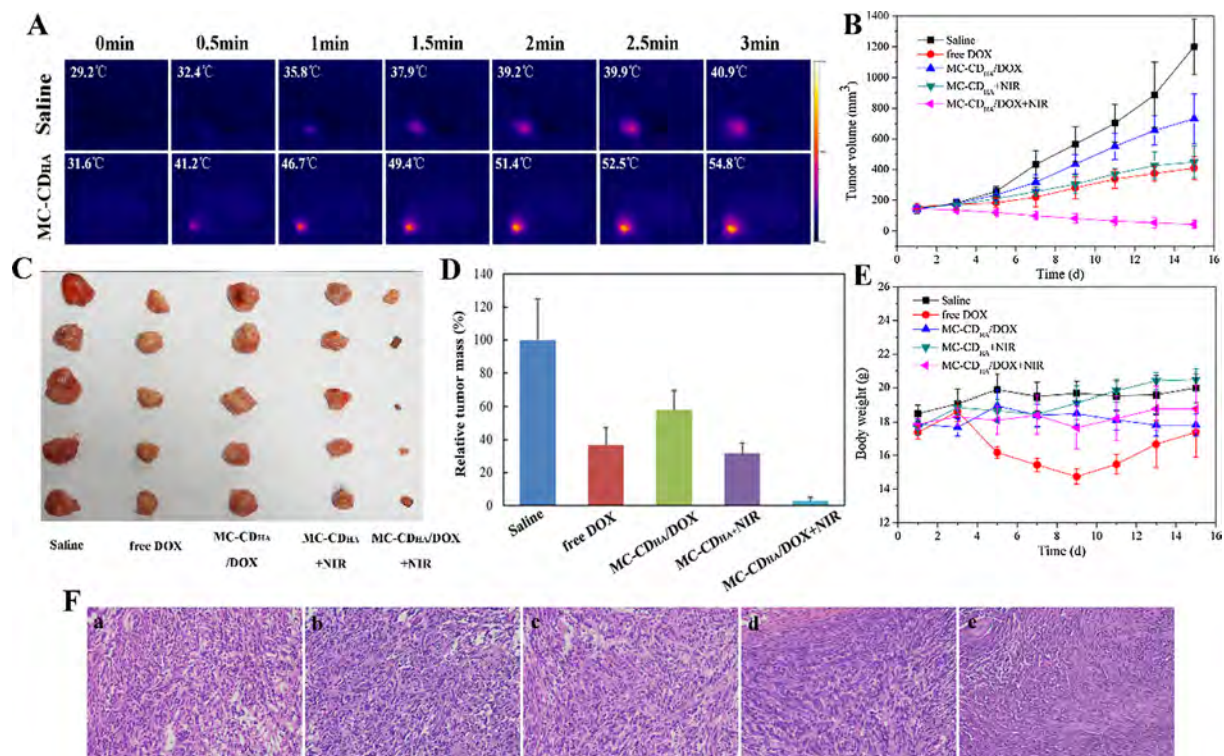


Fig. 7. (A) Infrared thermal images of tumor-bearing mouse after injection of PBS and MC-CD_{HA} under 808 nm NIR laser irradiation; (B) tumor growth curves of mice after various treatments (n = 5); (C) images of excised tumors after various treatments; (D) relative tumor weight (n = 5); (E) body weight variation of mice (n = 5); (F) H & E stained images of the tumors for each treatment group (a–e represent saline, free DOX, MC-CD_{HA}/DOX, MC-CD_{HA} + NIR, and MC-CD_{HA}/DOX + NIR).

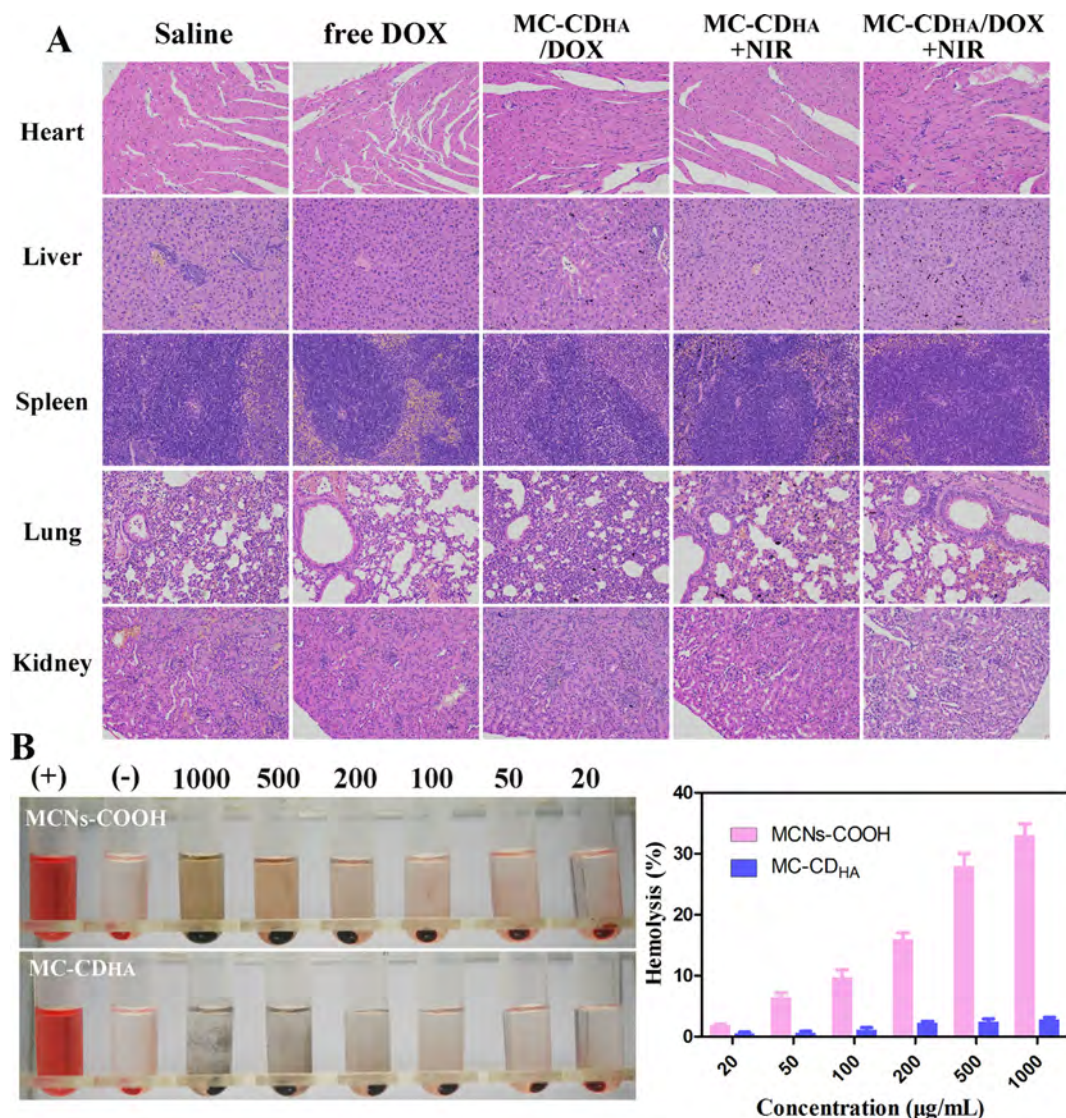


Fig. 8. (A) H&E staining of major tissues (heart, liver, spleen, lung and kidney) at the endpoint of antitumor efficacy study; (B) photographs and hemolysis percentage of MCNs-COOH and MC-CD_{HA} (n = 3).

mor activity of MC-CD_{HA}/DOX in vivo. The 4T1 mammary adenocarcinoma model was selected to validate the combination therapy. As shown in Fig. 7A, the temperature change and infrared thermal imaging of the tumor areas were monitored through an IR thermal camera. After 3 min of consecutive irradiation, for the MC-CD_{HA} group, the temperature of the tumor was increase from 31.6 to 54.8 °C, which was sufficient to ablate the tumor as well as trigger drug release, while the saline group exhibited a mild temperature change. As shown in Fig. 7B–D, rapid tumor growth was observed in the saline group, while moderately inhibited tumor growth was achieved using MC-CD_{HA}/DOX, which was attributed to the inadequate release of DOX from the nanoparticles. The tumors of the MC-CD_{HA}/DOX + NIR group were effectively suppressed due to the synergistic effect of chemotherapy and PTT. To clarify, the elevated temperature induced by near-infrared light accelerated DOX release to maximize chemotherapy. We observed the second best antitumor effect in the free DOX and MC-CD_{HA} + NIR groups. Additionally, the weights of mice, except for in the case of free DOX, did not show obvious differences for all of the groups during the entire treatment period (Fig. 7E), indicating there was no major toxicity of these treatments. To further evaluate the therapeutic effect of all groups, mice were sacrificed

at 15 d, and then, tumors were removed for H&E staining. The images of H&E stained tumor sections exhibited considerably enhanced necrosis for the MC-CD_{HA} + NIR group compared with the saline groups (Fig. 7F).

To estimate the potential toxicity effects on major organs, histological analyses of the heart, liver, spleen, lung and kidney stained with H&E were performed after treatments (Fig. 8A). There were no evident pathological changes in all treatments, except for the free DOX group, which exhibited obvious cardio toxicity. In addition, hemocompatibility studies were carried out to verify the safety of MC-CD_{HA}. The images and percentages of hemolysis of MCNs-COOH and MC-CD_{HA} are shown in Fig. 8B. The hemolysis percentage of MC-CD_{HA} was low, even at the highest concentration. These results suggested that MC-CD_{HA}/DOX had no noticeable toxicity in vivo and may hold promising potential for cancer treatment.

4. Conclusions

In summary, we fabricated a drug delivery system (MC-CD_{HA}/DOX) with tumor-targeted, multi-stimuli responsive and multi-modality imaging abilities for cancer treatment. Compared with

Au nanorods ($\eta = 21\%$) [50], MCNs-COOH were synthesized with a high photothermal conversion ability ($\eta = 27.4\%$). The fluorescent CD_{HA} modified on the surface of MCNs-COOH prevents premature drug release and enables targeted drug delivery to tumor cells and visualization of the location of drug release. The in vitro release results indicated that the drug release of MC-CD_{HA}/DOX could be triggered by pH, GSH and HAase and was further accelerated under NIR light irradiation. The key improvements in this work are that the system combined targeting ability with drug release visualization, which makes it feasible for monitor the location of nanoparticles and accurately killing cancer cells [51,52]. The resultant MC-CD_{HA}/DOX exhibited high stability, biosafety and an excellent synergistic treatment efficacy both in vitro and in vivo. Based on the above results, the unique multifunctional MC-CD_{HA}/DOX provides an intriguing nanoplatform for thermo-chemotherapy, which will undoubtedly represent an intelligent approach for precise cancer therapy.

Acknowledgements

This work was supported by National Natural Science Foundation of China (NO. 81603058 and 81473165).

Declaration of Competing Interest

We have no conflicts of interest.

Appendix A. Supplementary data

Supplementary data to this article can be found online at <https://doi.org/10.1016/j.jcis.2019.05.085>.

References

- [1] J. Shi, L. Wang, J. Zhang, R. Ma, J. Gao, Y. Liu, C. Zhang, Z. Zhang, *Biomaterials* 35 (2014) 5847.
- [2] H.-C. Hsu, C.-Y. Chen, M.-F. Chen, *J. Biomed. Sci.* 21 (2014) 101.
- [3] L. Cheng, J. Liu, X. Gu, H. Gong, X. Shi, T. Liu, C. Wang, X. Wang, G. Liu, H. Xing, *Adv. Mater.* 26 (2014) 1886.
- [4] J. Shi, Y. Liu, L. Wang, J. Gao, J. Zhang, X. Yu, R. Ma, R. Liu, Z. Zhang, *Acta Biomater.* 10 (2014) 1280.
- [5] N. Anikeeva, Y. Sykulev, E.J. Delikatny, A.V. Popov, *Am. J. Nucl. Med. Mol. Imag.* 4 (2014) 507.
- [6] Y. Liu, X. Yang, Z. Huang, P. Huang, Y. Zhang, L. Deng, Z. Wang, Z. Zhou, Y. Liu, H. Kalish, *Angew. Chem.* 128 (2016) 15523.
- [7] I. Schick, S. Lorenz, D. Gehrig, A.-M. Schilman, H. Bauer, M. Panthöfer, K. Fischer, D. Strand, F. Laquai, W. Tremel, *J. Am. Chem. Soc.* 136 (2014) 2473.
- [8] M. Feyen, C. Weidenthaler, F. Schüth, A.-H. Lu, *J. Am. Chem. Soc.* 132 (2010) 6791.
- [9] X. Li, L. Zhou, Y. Wei, A.M. El-Toni, F. Zhang, D. Zhao, *J. Am. Chem. Soc.* 136 (2014) 15086.
- [10] J.F. Lovell, T.W. Liu, J. Chen, G. Zheng, *Chem. Rev.* 110 (2010) 2839.
- [11] H. Yu, J. Li, D. Wu, Z. Qiu, Y. Zhang, *Chem. Soc. Rev.* 39 (2010) 464.
- [12] B.P. Timko, T. Dvir, D.S. Kohane, *Adv. Mater.* 22 (2010) 4925.
- [13] P. Huang, J. Lin, X. Wang, Z. Wang, C. Zhang, M. He, K. Wang, F. Chen, Z. Li, G. Shen, *Adv. Mater.* 24 (2012) 5104.
- [14] P. Klán, T.S. Šolomek, C.G. Bochet, A.L. Blanc, R. Givens, M. Rubina, V. Popik, A. Kostikov, J. Wirz, *Chem. Rev.* 113 (2012) 119.
- [15] L. Cheng, C. Wang, L. Feng, K. Yang, Z. Liu, *Chem. Rev.* 114 (2014) 10869.
- [16] G. Liu, W. Liu, C.-M. Dong, *Polym. Chem.* 4 (2013) 3431.
- [17] Z. Gu, L. Yan, G. Tian, S. Li, Z. Chai, Y. Zhao, *Adv. Mater.* 25 (2013) 3758.
- [18] J.-F. Gohy, Y. Zhao, *Chem. Soc. Rev.* 42 (2013) 7117.
- [19] H. Wang, Y.-L. Zhao, G.-J. Nie, *Front. Mater. Sci.* 7 (2013) 118.
- [20] W. Zhang, Z. Guo, D. Huang, Z. Liu, X. Guo, H. Zhong, *Biomaterials* 32 (2011) 8555.
- [21] X. Qin, Z. Guo, Z. Liu, W. Zhang, M. Wan, B. Yang, *J. Photochem. Photobiol., B* 120 (2013) 156.
- [22] M. O'Connell, J.A. Wisdom, H. Dai, H.B. Gray, *PNAS* 102 (2005) 11600.
- [23] P. Chakravarty, R. Marches, N.S. Zimmerman, A.D.-E. Swafford, P. Bajaj, I.H. Musselman, P. Pantano, R.K. Draper, E.S. Vitetta, *Proc. Natl. Acad. Sci.* 105 (2008) 8697.
- [24] J.W. Fisher, S. Sarkar, C.F. Buchanan, C.S. Szot, J. Whitney, H.C. Hatcher, S.V. Torti, C.G. Rylander, M.N. Rylander, *Cancer Res.* 70 (2010) 9855.
- [25] K. Yang, S. Zhang, G. Zhang, X. Sun, S.-T. Lee, Z. Liu, *Nano Lett.* 10 (2010) 3318.
- [26] W.S. Seo, J.H. Lee, X. Sun, Y. Suzuki, D. Mann, Z. Liu, M. Terashima, P.C. Yang, M. V. McConnell, D.G. Nishimura, *Nat. Mater.* 5 (2006) 971.
- [27] S.P. Sherlock, S.M. Tabakman, L. Xie, H. Dai, *ACS Nano* 5 (2011) 1505.
- [28] L. Zhou, K. Dong, Z. Chen, J. Ren, X. Qu, *Carbon* 82 (2015) 479.
- [29] F. Xu, Z. Tang, S. Huang, L. Chen, Y. Liang, W. Mai, H. Zhong, R. Fu, D. Wu, *Nat. Commun.* 6 (2015).
- [30] J. Liu, N.P. Wickramaratne, S.Z. Qiao, M. Jaroniec, *Nat. Mater.* 14 (2015) 763.
- [31] L. Zhou, Y. Jing, Y. Liu, Z. Liu, D. Gao, H. Chen, W. Song, T. Wang, X. Fang, W. Qin, *Theranostics* 8 (2018) 663.
- [32] T. Wang, D. Wang, H. Yu, M. Wang, J. Liu, B. Feng, F. Zhou, Q. Yin, Z. Zhang, Y. Huang, *ACS Nano* 10 (2016) 3496.
- [33] J. Zhang, Z.F. Yuan, Y. Wang, W.H. Chen, G.F. Luo, S.X. Cheng, R.X. Zhuo, X.Z. Zhang, *J. Am. Chem. Soc.* 135 (2013).
- [34] N. Mas, A. Agostini, L. Mondragón, A. Bernardos, F. Sancenon, M.D. Marcos, R. Martínez-Mañez, A.M. Costero, S. Gil, M. Merino-Sanjuán, *Chem.—A Euro. J.* 19 (2013) 1346.
- [35] Y. Qin, J. Chen, Y. Bi, X. Xu, H. Zhou, J. Gao, Y. Hu, Y. Zhao, Z. Chai, *Acta Biomater.* 17 (2015) 201.
- [36] Z. Zhang, J. Wang, X. Nie, T. Wen, Y. Ji, X. Wu, Y. Zhao, C. Chen, *J. Am. Chem. Soc.* 136 (2014) 7317.
- [37] H. Lea-Banks, M. O'reilly, K. Hynynen, *J. Contr. Rel.* (2018).
- [38] J. Zhan, Z. Ma, D. Wang, X. Li, X. Li, L. Le, A. Kang, P. Hu, L. She, F. Yang, *Int. J. Nanomed.* 12 (2017) 2733.
- [39] A. Zhu, K. Miao, Y. Deng, H. Ke, H. He, T. Yang, M. Guo, Y. Li, Z. Guo, Y. Wang, *ACS Nano* 9 (2015) 7874.
- [40] W. Xiao, Y. Li, C. Hu, Y. Huang, Q. He, H. Gao, *J. Colloid Interface Sci.* 497 (2017) 226.
- [41] L. Pan, S. Sun, A. Zhang, K. Jiang, L. Zhang, C. Dong, Q. Huang, A. Wu, H. Lin, *Adv. Mater.* 27 (2015) 7782.
- [42] H. Wang, J. Di, Y. Sun, J. Fu, Z. Wei, H. Matsui, A. Del, C. Alonso, S. Zhou, *Adv. Funct. Mater.* 25 (2015) 5537.
- [43] Y. Lv, C. Xu, X. Zhao, C. Lin, X. Yang, X. Xin, L. Zhang, C. Qin, X. Han, L. Yang, *ACS Nano* 12 (2018) 1519.
- [44] X. Li, Y. Yan, Y. Lin, J. Jiao, D. Wang, D. Di, Y. Zhang, T. Jiang, Q. Zhao, S. Wang, *J. Colloid Interface Sci.* 494 (2017) 159.
- [45] W.Z. Song, Y.Z. Li, Y.Q. Wang, D.Z. Wang, D. He, W. Chen, W.Z. Yin, W.S. Yang, *J. Biomed. Nanotechnol.* 13 (2017) 1115.
- [46] Y. Lv, C. Xu, X. Zhao, C. Lin, X. Yang, X. Xin, L. Zhang, C. Qin, X. Han, L. Yang, *ACS Nano* 12 (2018).
- [47] F. Mirab, Y.J. Kang, S. Majd, *PLoS One* 14 (2019) e0211078.
- [48] J. Yang, H. Su, W. Sun, J. Cai, S. Liu, Y. Chai, C. Zhang, *Theranostics* 8 (2018) 1966.
- [49] L. Jie, L. Monty, L. Zongxi, J.I. Zink, T. Fuyuhiko, *Small* 6 (2010) 1794.
- [50] C.M. Hessel, V.P. Pattani, M. Rasch, M.G. Panthani, B. Koo, J.W. Tunnell, B.A. Korgel, *Nano Lett.* 11 (2011) 2560.
- [51] Z. Li, D. Kai, Z. Chen, J. Ren, X. Qu, *Carbon* 82 (2015) 479.
- [52] R. Lima-Sousa, D. de Melo-Diogo, C.G. Alves, E.C. Costa, P. Ferreira, R.O. Louro, I. J. Correia, *Carbohydr. Polym.* 200 (2018) 93.